Dissociative ionization and Coulomb explosion of CH_4 in two-color asymmetric intense laser fields

Journal:	*Physical Chemistry Chemical Physics*
Manuscript ID	CP-ART-05-2023-002337.R1
Article Type:	Paper
Date Submitted by the Author:	10-Aug-2023
Complete List of Authors:	Hasegawa, Hiroka; Nagoya University School of Science Graduate School of Science, Matsuda, Akitaka; Nagoya University, Department of Chemistry Morishita, Toru; University of Electro Communications Faculty of Informatics and Engineering Madsen, Lars; Aarhus Universitet, Physics and Astronomy Jensen, Frank; Aarhus University, Department of Chemistry Tolstikhin, Oleg; Moscow Institute of Physics and Technology National Research University, Hishikawa, Akiyoshi; Nagoya University, Department of Chemistry, Graduate School of Science; Nagoya University, Research Center for Materials Science

CH4 w2w/PCCP2023

Dissociative ionization and Coulomb explosion of CH_4 in two-color asymmetric intense laser fields

H. Hasegawa,[1] A. Matsuda,[1] T. Morishita,[2] L. B. Madsen,[3]
F. Jensen,[4] O. I. Tolstikhin,[5] and A. Hishikawa[1, 6, *]

[1] *Graduate School of Science, Nagoya University,*
Furo-cho, Chikusa, Nagoya, Aichi, 464-8602, Japan
[2] *Institute for Advanced Science, The University of Electro-Communications,*
1-5-1 Chofu-ga-oka, Chofu-shi, Tokyo 182-8585, Japan
[3] *Department of Physics and Astronomy,*
Aarhus University, 8000 Aarhus C, Denmark
[4] *Department of Chemistry, Aarhus University, 8000 Aarhus C, Denmark*
[5] *Moscow Institute of Physics and Technology, Dolgoprudny 141700, Russia*
[6] *Research Center for Materials Science, Nagoya University,*
Furo-cho, Chikusa, Nagoya, Aichi, 464-8602, Japan

(Dated: August 25, 2023)

Abstract

Directional fragment ejection from a tetrahedral molecule CH_4 in linearly polarized two-color (ω and 2ω) asymmetric intense laser fields (50 fs, 1.4×10^{14} W/cm^2, 800 nm and 400 nm) has been studied by three-dimensional ion coincidence momentum imaging. The H^+ fragment produced from dissociative ionization, $CH_4 \to H^+ + CH_3 + e^-$, is preferentially ejected on the larger amplitude side of the laser electric fields. Comparison with theoretical predictions by weak-field asymptotic theory shows that the observed asymmetry can be understood by the orientation selective tunneling ionization from the triply degenerated highest occupied molecular orbital ($1t_2$) of CH_4. A similar directional ejection of H^+ was also observed for the low kinetic energy components of the two-body Coulomb explosion, $CH_4 \to H^+ + CH_3^+ + 2e^-$. On the other hand, the fragment ejection in the opposite direction were observed for the high energy component, as well as H_2^+ produced from the Coulomb explosion $CH_4 \to {H_2}^+ + CH_2^+ + 2e^-$. Possible origins of the characteristic fragmentation are discussed.

I. INTRODUCTION

Intense laser pulses have large electric fields comparable to intramolecular Coulomb fields, driving ultrafast dynamics of electrons within atoms and molecules. The atomic and molecular responses are thus sensitive to how the electric field varies in time, that is, the waveform of the laser electric field. A number of studies have been carried out to investigate the applicability of waveform shaping to control chemical reactions in the intense field regime. In order to explore the pulse shape to maximize a certain reaction channel, machine learning techniques based on, e.g., genetic algorithm, have been adopted. They have been successfully applied to selective bond breaking and bond rearrangement of small molecules [1–7]. The carrier-envelope-phase (CEP) locked few-cycle pulse [8, 9] utilizes the CEP as a tuning knob to manipulate the electric field waveform, which varies by the phase between the carrier wave and the envelope. The CEP-locked few-cycle pulses are utilized to control electron localization of H_2^+ [10, 11], and D_2^+ [11–14] during the dissociative ionization $H_2 \to H^+ + H + e^-$ ($D_2 \to D^+ + D + e^-$). The fragment ejection from C_2H_2 [15] also showed asymmetry along the laser polarization direction depending on the CEP.

Another approach is to use frequency mixing to the waveform shaping. The two-color, ω-2ω laser fields, consisting of two laser pulses with the fundamental and the second harmonic

---

* hishi@chem.nagoya-u.ac.jp

frequencies is one such laser pulse, where the relative phase ϕ between the two fields is used as a control parameter. In the case of linear polarization along the Z direction, the ω-2ω electric fields may be expressed as,

$$\mathbf{F}(t) = F(t)\mathbf{e}_Z, \tag{1}$$

$$F(t) = \bar{F}_\omega(t)\cos(\omega t) + \bar{F}_{2\omega}(t)\cos(2\omega t + \phi), \tag{2}$$

where $\bar{F}_\omega(t)$ and $\bar{F}_{2\omega}(t)$ represent the envelopes of the fundamental and the second harmonic pulses, respectively. The unit vector along the Z-axis is denoted as $\mathbf{e}_Z$. Typical ω-2ω electric fields are illustrated in Fig. 1. The waveform is characterized with the directional electric fields, whose asymmetry varies by the phase ϕ for a given ratio of the ω and 2ω field intensities.

The ω-2ω laser pulses have been widely used for understanding laser tunneling ionization and dissociation in intense laser fields [16, 17]. In particular, asymmetric fragment ejections from symmetric molecules were observed for small molecules, such as D_2 [18, 19], CO_2 [20, 21], C_2H_2 [22], and H_2O [23, 24]. The origin of the asymmetry has been discussed in terms of coherent coupling between electronic states [18, 19], laser-induced coupling of highest-occupied molecular orbitals (HOMO) and HOMO-1, 2 [22], and the wavepacket dynamics on deformed potential energy surface (PES) [20, 21].

Recently, we carried out an ω-2ω study on dissociative tunneling ionization of tetrafluoromethane (CF_4), which has repulsive potential energy surfaces in the ground and first excited states of CF_4^+. It was shown that the asymmetric ejection of the CF_3^+ fragment shows a phase shift of $\sim \pi$ with respect to the prediction by the tunneling ionization from HOMO ($1t_1$) and HOMO-1 ($4t_2$) [25]. The coupling between the two lowest electronic states [26] is suggested as a possible origin of the discrepancy, indicating the importance of post-ionization effect in ultrafast dissociative ionization associated with the energy difference close to the photon energy of the fundamental pulse (800 nm).

In this study, another tetrahedral molecule CH_4, one of the simplest hydrocarbons, is investigated. The electron configuration of CH_4 in its ground state is $(1a_1)^2(2a_1)^2(1t_2)^6$. The energy difference between the $1t_2$ and $2a_1$ orbitals is large ($\sim$ 8 eV) enough to suppress the coupling by laser fields observed in the CF_4 study. Furthermore, it is known that methane has a dissociation process involving H-H bond formation to produce H_2^+. Two dissociative ionization (DI) pathways in ω-2ω intense laser fields (50 fs, 1.4×10^{14} W/cm^2),

$$\text{(i)} \quad CH_4 \rightarrow H + CH_3^+ + e^-, \tag{3}$$

$$\text{(ii)} \quad CH_4 \rightarrow H^+ + CH_3 + e^-, \tag{4}$$

from singly charged methane (CH_4^+), and two Coulomb explosion (CE) pathways,

$$\text{(I)} \quad CH_4 \rightarrow H^+ + CH_3^+ + 2e^-, \tag{5}$$

$$\text{(II)} \quad CH_4 \rightarrow H_2^+ + CH_2^+ + 2e^-, \tag{6}$$

are identified in addition to a minor CE pathway $CH_4 \rightarrow H_3^+ + CH^+ + 2e^-$ by using three-dimensional ion momentum imaging. The directional ejection and its phase dependence are discussed in terms of the ionization and dissociation dynamics in the ω-2ω intense laser fields.

The paper is organized as follows. Section II describes the experimental setup for the three-dimensional momentum imaging of the fragment ions from CH_4 in linearly polarized ω-2ω intense laser fields (1.4×10^{14} W/cm^2, 800 nm and 400 nm). The dissociative ionization pathways from CH_4^+ are discussed in Section III. The observed fragment asymmetry is compared with theoretical predictions by the weak-field asymptotic theory (WFAT) [27] for tunneling ionization in Section IV. Finally, Section V presents the phase dependence of the CE processes from CH_4^{2+}, where possible processes contributing to the two different pathways, e.g., rescattering of tunneling electrons and post-ionization interactions, are discussed.

II. EXPERIMENTAL SETUP

The schematic of the experimental setup is shown in Fig.1. The output from a Ti:Sapphire regenerative laser amplifier system (800 nm, 1 kHz, 50 fs) was introduced to an inline ω-2ω pulse generator [21, 28]. After generation of the second-order harmonics (400 nm, $\sim$70 fs) by a type-I β-BBO crystal, the coarse time delay between the ω and 2ω pulses was compensated by two birefringent α-BBO crystals. The fine tuning of the time delay was accomplished by a pair of fused-silica wedge plates. The relative phase of the two-color laser pulses was stabilized by the active feedback control of the wedge plate utilizing the 2ω-2ω interference spectrum. The polarization direction of the fundamental and the second harmonic pulses was set parallel with each other by a true zero-order dual-wavelength wave plate.

The ω-2ω laser pulse was introduced into an ultrahigh vacuum chamber and was focused onto an effusive molecular beam by a focusing mirror (f = 75 mm). Fragment ions generated by the

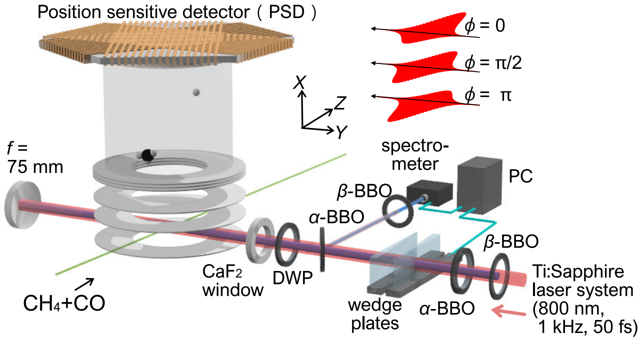

FIG. 1. Schematic of the experimental setup consisting of an inline ω-2ω pulse generator and an ion coincidence momentum imaging system equipped with a delay-line anode position sensitive detector [25]. The output from a Ti:Sapphire regenerative laser amplifier is introduced to a β-BBO crystal (type-I). The time delay between the fundamental (ω) and the second harmonic (2ω) pulse was compensated by two birefringent α-BBO crystals. A pair of fused-silica wedge plates was used for control of the two-color relative phase which was stabilized by the active feedback loop utilizing the 2ω-2ω interference spectrum. The polarization of the fundamental and the second harmonic pulse was set parallel to the Z-axis of the laboratory frame by a dual-wavelength waveplate (DWP). The inset to the top right shows the waveform dependence on the relative phase ϕ.

interaction with ω-2ω intense laser fields were guided to a delay-line anode position-sensitive detector (PSD) by a static electric field (68.2 V/cm). The three-dimensional momentum (p_X, p_Y, p_Z) of each fragment ion was obtained from the arrival position (Y, Z) at the detector and the time of flight (t).

The peak intensity on the target gas was 1.4×10^{14} W/cm^2, which was determined by separate measurements using circularly polarized femtosecond laser pulse [29]. The intensity ratio of the fundamental I_ω and the second harmonics $I_{2\omega}$ was estimated to be $I_{2\omega}\ /I_\omega = 0.14$ from the laser power ratio measured in front of the vacuum chamber window. A mixture of CH_4 and CO was used as the sample gas. The absolute phase difference ϕ between ω and 2ω pulses at the focal point was determined by the phase dependence of the directional ejection of C^+ from Coulomb explosion of CO [30].

In order to identify the Coulomb explosion pathways, the coincidence momentum imaging technique is applied [31]. The fragment ions generated by a single laser pulse can be detected by coincidence measurement. In the present study, the number of signals per pulse is around 0.7. The

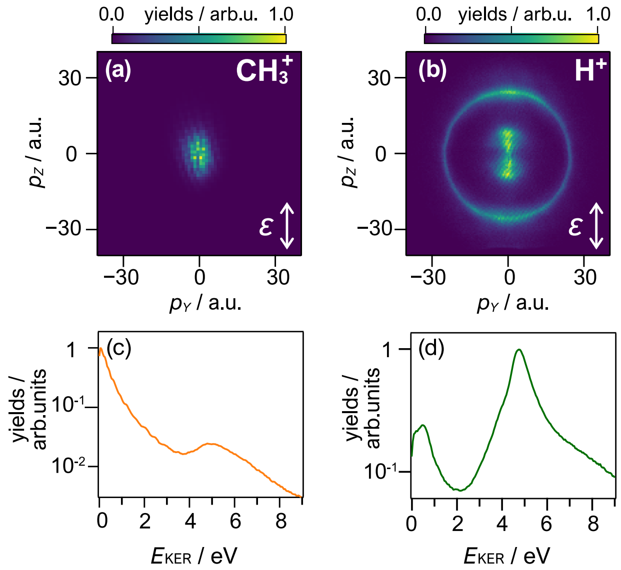

FIG. 2. Phase-averaged momentum images on the $p_Y - p_Z$ plane of (a) CH_3^+ and (b) H^+ fragment ions, obtained by the integration over $|p_X| \leq 3$ a.u.. The arrows with ε represent the direction of the laser polarization. Kinetic energy release spectra E_{KER} in logarithmic scale, which are obtained from the momenta of (c) CH_3^+ and (d) H^+, respectively. Two-body dissociation and the momentum conservation with the counterpart fragment are assumed.

detected ions may originate in different molecules. To eliminate false coincidences, a constraint from the momentum conservation law $|\sum_i \mathbf{p}_i|^2/\sum_i |\mathbf{p}_i|^2 < 0.15$ was used for Coulomb explosion processes (I) and (II) in Eqs.(5) and (6) to separate true coincidence events from false events.

III. DISSOCIATIVE TUNNELING IONIZATION

In this section we consider the dissociative ionization processes (i) and (ii) in Eqs.(3) and (4). Figures 2 (a) and (b) show the two-dimensional momentum images of the CH_3^+ and H^+ fragments on the $p_Y - p_Z$ plane, which are obtained as the averages of the corresponding ion images recorded at different relative phases ϕ. The momentum image of CH_3^+ is dominated by a strong component peaked at the center. It should be noted that the initial velocity of CH_4 molecular beam along the Z-axis, which is parallel to the laser polarization direction, also contributes to the momentum distribution of the fragment ions. On the other hand, the H^+ ion image is characterized by two distinct features at $|\mathbf{p}| \leq 15$ a.u. and $|\mathbf{p}| \sim 25$ a.u. The coincidence measurements (Section V A)

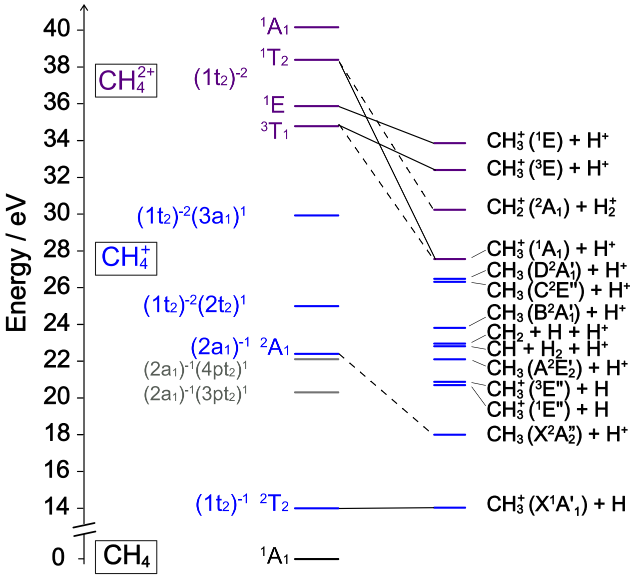

FIG. 3. Energy level diagram of selected electronic states of CH_4, CH_4^+ [32] and CH_4^{2+} [33], at the equilibrium geometry of CH_4 in the ground state. The energy levels of product states [34, 35] are also shown. Directly correlated parent and product states are connected by solid lines. Pathways identified in the previous studies [32, 36–38] are indicated by dotted lines.

show that the latter originates from the two-body CE pathway (I) in Eq.(5). The former is therefore assigned to dissociative ionization producing the H^+ fragments by pathway (ii) in Eq.(4). The H^+ fragment ion from the pathway (ii) is ejected mostly along the laser polarization direction with the anisotropy parameter of $\langle \cos^2\theta \rangle = 0.62$, while CH_3^+ from pathway (i) exhibits more isotropic distribution.

From the measured momenta $\mathbf{p}_{CH_3^+}$, the total kinetic energy release (KER) can be calculated for the two-body fragmentation processes. By using the momentum conservation with the counterpart fragment, KER can be expressed as $E_{\mathrm{KER}} = |\mathbf{p}|^2/(2\mu)$, where $\mu = m_{\mathrm{H}} m_{\mathrm{CH_3}}/(m_{\mathrm{H}} + m_{\mathrm{CH_3}})$ is the reduced mass. The obtained KER spectrum for the CH_3^+ is shown in Fig.2(c), which shows that a strong component peaked at 0 eV appears together with a small peak at 5.0 eV, associated with the Coulomb explosion pathway (I). Figure 2(d) shows the KER spectrum for pathway (ii) calculated in the same manner, which shows two peaks at 0.5 eV and 4.8 eV with a shoulder-like feature on the lower energy side of the former.

A. H + CH_3^+ pathway

Dissociative ionization of CH_4 has been subjected to a number of studies, including those in intense laser fields [39–41]. The electronic states relevant to the present study are shown in Fig.3. An electron impact study [42] showed that the appearance energy of CH_3^+ is 14.01 eV, which is slightly above the ionization threshold 12.63 eV to CH_4^+ [42]. The formation of the CH_3^+ fragment is attributed to the direct dissociation from the ground state of CH_4^+. The electronic ground state X^2T_2 $(1t_2)^{-1}$ of CH_4^+ is a metastable state having a long dissociation lifetime ($\sim \mu$s) [43]. Statistical dissociation [39, 44] and rotational barrier tunneling [45] were suggested as the dissociation mechanisms. The vibrationally and rotationally excited CH_4^+ in the ground state dissociate to CH_3^+ (X^1A_1') + H with a small kinetic energy (<0.6 eV) for CH_3^+ [46], as observed in the present study. The Jahn-Teller distortion is suggested to contribute to the metastable state reaction leading to predissociation via the triply degenerated $^2T_2$ state [47].

To evaluate the asymmetry of the fragment distribution along the ω-2ω laser polarization direction, the asymmetry parameter $A(\phi)$,

$$A(\phi) = \frac{Y_+(\phi) - Y_-(\phi)}{Y_+(\phi) + Y_-(\phi)}, \tag{7}$$

is introduced. Here, Y_+ and Y_- represent the ion yields with positive and negative momenta within a 45° acceptance angle along the laser polarization direction (Z-axis) at a given relative phase ϕ.

Figure 4(b) plots the asymmetry parameter observed for CH_3^+, showing a weak but clear dependence on the relative phase ϕ. The asymmetric ejection of CH_3^+ is confirmed in the KER dependent asymmetric parameter,

$$A(\phi, E_{\mathrm{KER}}) = \frac{Y_+(\phi, E_{\mathrm{KER}}) - Y_-(\phi, E_{\mathrm{KER}})}{Y_+(\phi, E_{\mathrm{KER}}) + Y_-(\phi, E_{\mathrm{KER}})}. \tag{8}$$

which is shown in Fig. 4 (c) together with the corresponding KER spectrum [Fig. 4 (a)]. Interestingly, the asymmetry parameter of the parent ion shows a similar phase-dependence (see Supplementary Materials). This is attributed to the momentum recoil from the tunneling electron, which is known to show an asymmetric momentum distribution in two-color laser fields [22]. The momentum recoil effect becomes substantial for the fragment ions with small kinetic energies. Indeed, the asymmetry parameter of CH_3^+ obtained after correction for the momentum recoil has significantly small values, showing that the apparent fragment asymmetry is attributed essentially to the electron momentum recoil. The small asymmetry can be attributed to the molecular rotation before dissociation, which smears out the effect of the asymmetric laser fields.

B. H^+ + CH_3 pathway

The previous ion-electron coincidence study of H^+ from methane by 54 eV electron impact shows a broad kinetic energy spectrum peaked at below 0.5 eV [32], which is consistent with the present KER spectrum shown in Fig.2(d). This low energy proton was assigned to the dissociation from CH_4^+ $(1t_2)^{-2}(3a_1)^1$. In the present case, such excited states can be produced by tunneling ionization from the HOMO $(1t_2)$ and the subsequent excitation by the laser fields or by electron rescattering which promotes another electron from $1t_2$ to $3a_1$. Indeed, the ponderomotive energy of the ω laser field is 8.4 eV under the present experimental conditions. The maximum value of the electron rescattering energy in the ω field is $3.17U_p \sim 27$ eV, which exceeds the energy (17 eV) required to excite $(1t_2)^{-2}(3a_1)^1$ states from the ground state of CH_4^+.

The electron impact study [32] also identified an additional peak at ~0.1 eV in the proton kinetic energy spectrum, which was assigned to the dissociation from the autoionizing states in the $(2a_1)^{-1}(npt_2)^1(n=3,4)$ configuration. This may explain the shoulder-like feature on the lower energy side of the peak at 0.5 eV in the KER spectrum in Fig.2(d), if the tunnel electron from HOMO-1 $(2a_1)$ can be efficiently captured to the autoionizing states by the rescattering. On the other hand, the asymmetry parameters for H^+ are shown in Fig.5(b), which exhibits a clear phase dependence with an amplitude exceeding 0.1. Figure 5(c) shows the dependence on KER [see Fig. 5 (a)]. The asymmetry parameter is almost independent of KER in the most of the range investigated ($E_{\mathrm{KER}} < 2$ eV), which is consisted with the assignment of the dissociation pathway from CH_4^+ in the $(1t_2)^{-2}(3a_1)^1$ excited states. The asymmetry parameter also shows a phase shift of $\sim \pi$ below 0.2 eV. This can be attributed to contributions of other dissociation pathways, such as that from the $(2a_1)^{-1}(npt_2)^1(n=3,4)$ autoionizing states mentioned above.

The asymmetry parameters for these KER regions are also plotted in Fig.5 (b). The results of the least-squares fitting to a cosine function,

$$A(\phi) = A_0 \cos(\phi - \phi_0), \tag{9}$$

are also shown. The amplitude and phase were obtained to be A_0 = 0.05(1), ϕ_0 = 1.3(1) π for E_{KER} = 0-0.2 eV, while A_0 = 0.13(1), ϕ_0 = −0.1(1) π for E_{KER} = 0.2-2 eV, where the number in the parentheses represents the uncertainty in the last digit. This shows that H^+ produced from the major component at E_{KER} = 0.2-2 eV is preferentially ejected to the larger amplitude side of the ω-2ω laser electric fields.

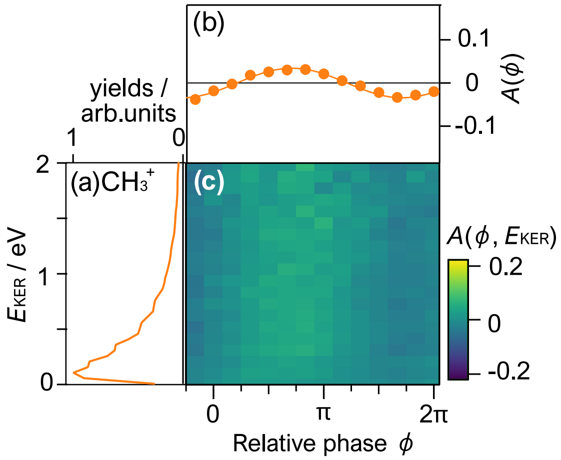

FIG. 4. (a) KER spectra for the dissociative ionization pathway (i). (b) KER integrated asymmetry parameter, $A(\phi)$ in Eq.(7), for CH_3^+. Solid line is the result of the least-squares fitting to cosine functions in Eq.(9). The statistical uncertainties are smaller than the size of the markers. (c) Two-dimensional plot of the asymmetry parameter, $A(\phi, E_{KER})$ in Eq.(8), of CH_3^+. The fragment asymmetry is attributed essentially to the momentum recoil from the tunneling electron (see Supplementary materials).

IV. ORIENTATION DEPENDENT TUNNELING IONIZATION

A. Tunneling ionization rate

To understand the asymmetric ejection of H^+ from CH_4 in the ω-2ω intense laser fields, theoretical calculations of the tunneling ionization rate for the $1t_2$ HOMO were carried out by the weak-field asymptotic theory (WFAT) [27]. Briefly, the tunneling ionization rate in this approach is expressed as [48],

$$\Gamma(\beta,\gamma) = |G_{00}(\beta,\gamma)|^2 W_{00}(F), \tag{10}$$

where $G_{00}(\beta,\gamma)$ is the structure factor that describes the dependence on the molecular orientation relative to the laser electric field F defined by the Euler angles (α, β, γ) (see Fig.6) [49]. The field factor, $W_{00}(F)$, which defines the dependence on the field strength F, is given as,

$$W_{00}(F) = \frac{\varkappa}{2}\left(\frac{4\varkappa^2}{F}\right)^{2/\varkappa-1} \exp\left(-\frac{2\varkappa^3}{3F}\right), \tag{11}$$

where $\varkappa = \sqrt{-2E_0}$, with E_0 being the energy of the molecular orbital from which the electron is ionized. The subscript 00 refers to the dominant ionization channel [27, 48]. Note that atomic units are used in this section.

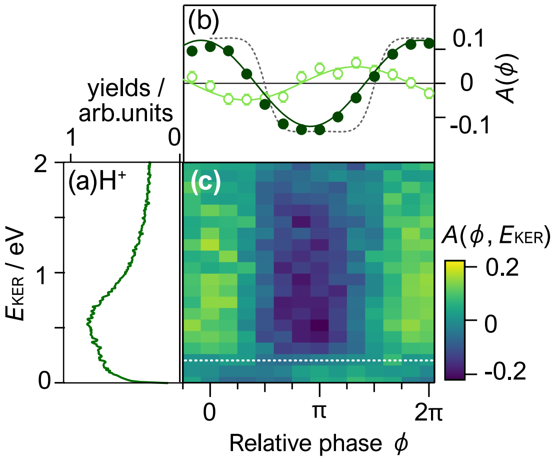

FIG. 5. (a) KER spectra for the dissociative ionization pathway (ii). (b) KER integrated asymmetry parameter, $A(\phi)$ in Eq.(7), for H^+ in the kinetic energy ranges $0 \leq E_{\mathrm{KER}} \leq 0.2$ eV (open circles) and $0.2 \leq E_{\mathrm{KER}} \leq 2$ eV (filled circles). The statistical uncertainties are smaller than the size of the markers. Solid lines are results of the least-squares fitting to cosine functions in Eq.(9). The dotted gray curve in (b) is a result of the tunneling ionization simulated asymmetry parameter for H^+ by weak-field asymptotic theory (WFAT) for tunneling ionization from the $1t_2$ HOMO. (c) Two-dimensional plot of the asymmetry parameter, $A(\phi, E_{\mathrm{KER}})$ in Eq.(8), for H^+.

The CH_4 molecule has three degenerate $1t_2$ HOMOs (Fig.7). The calculation involving triply degenerated molecular orbitals is described in our previous paper [25]. The Stark interaction with the ionizing field removes the degeneracy. Tunneling ionization occurs from eigenorbitals of the operator $-(\boldsymbol{\mu} \cdot \boldsymbol{F})$ within each degenerate subspace, where $\boldsymbol{\mu}$ is the electric dipole moment of the considered orbital [52]. The eigenorbitals that diagonalize the Stark term $(\boldsymbol{\mu} \cdot \boldsymbol{F})$ are given by linear combinations of the three degenerate HOMOs. The structure factors $G_{00}(\beta, \gamma)$ incorporating the effect of the dipole for the eigenorbitals are calculated using the integral representation of the WFAT [53–55] implemented in the GAMESS package with a polarization consistent basis set at the pc-4 level [56]. The orbitals are labeled as ϕ_{A}, ϕ_{B}, and ϕ_{C} in the ascending order of the dipole, $\mu_{\mathrm{A}} < \mu_{\mathrm{B}} < \mu_{\mathrm{C}}$. The orbital energy to the first order in the field is given as

$$E_{0,i}(\boldsymbol{F}) = E_0 - \boldsymbol{\mu}_i \cdot \boldsymbol{F}, \tag{12}$$

where $i = \mathrm{A}, \mathrm{B}, \mathrm{C}$. Figure 8 shows the energy of eigenorbitals calculated using Eq.(12) at four different molecular orientations with respect to $\boldsymbol{F}$.

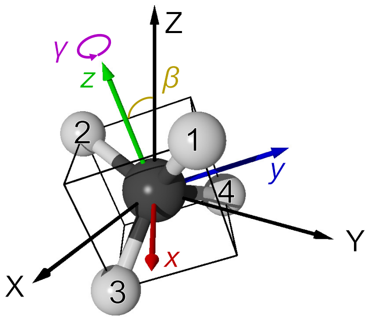

FIG. 6. Methane (CH_4) molecule in the ground state having T_d symmetry. The molecular principal axis (C_2 axis) is along the z-axis of the molecular frame (x, y, z). The orientation is specified by the Euler angles (α, β, γ) in the laboratory frame (X, Y, Z), which is defined to have the electric field along the Z-axis.

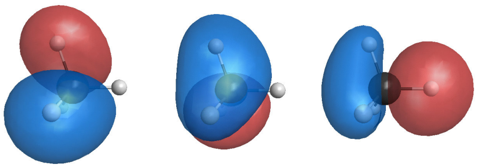

FIG. 7. Triply-degenerated highest-occupied molecular orbitals HOMO ($1t_2$) of CH_4. Optimized geometry calculated by GAMESS (US) package [50], HF aug-cc-pVQZ, and MO surface graphics are made by MacMolPlt program [51].

Figures 9(a)-(c) show the squared norms of the structure factors $|G_{00}(\beta,\gamma)|^2$ of ϕ_A, ϕ_B and ϕ_C, resulting from the triply degenerate HOMO ($E_0 = -14.8$ eV). Note that we set $\alpha = 0$ because the ionization rate is independent of α. The structure factors in Fig.9 (a)-(c) show that the largest contribution to the tunneling ionization comes from the eigenorbital ϕ_C which has the highest value of the maximum of $G_{00}(\beta,\gamma)$ because the field factor $W_{00}(F)$ is common for ϕ_A, ϕ_B and ϕ_C [see Eq.(11)].

The sum of the structure factors $\sum_i |G_{00,i}(\beta,\gamma)|^2$ ($i = \mathrm{A,B,C}$) are shown in Fig.9(d), which describes how the tunneling ionization rate varies with the molecular orientation when the three eigenorbitals are equally populated. For example, the electric field points from C to H at (β,γ) = (54°, 134°), while it points from H to C at (β,γ) = (124°, 314°). The tunneling ionization is enhanced by a factor of $\sim$2 when the electric field is pointing from C to H than the opposite orientation. This indicates that the orientation-selective tunneling ionization can occur for CH_4

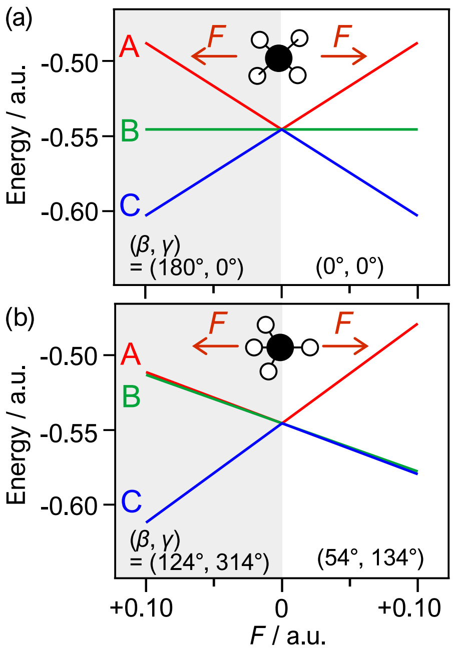

FIG. 8. Stark-shifted energies, $E_{0,i}(\boldsymbol{F})$, of eigenorbitals, ϕ_i, (i = A, B, C), of HOMO as a function of the static field F [see Eq.(12)] at four different molecular orientations with respect to F. (a) The electric field is parallel to the molecular principal axis (C_2), i.e., (β, γ) = (0°, 0°) (right) and (180°, 0°) (left). (b) Same as (a) but for (β, γ) = (54°,134°) (right) and (124°, 314°) (left), where the electric field is almost parallel to one of the C-H axes.

having a high symmetry (T_d) as has been discussed for CF_4 [25].

B. Fragment angular distribution

To obtain the asymmetry parameter, the angular distribution of H^+ fragment is calculated under an assumption that the breaking of each of the four equivalent C-H bonds occurs with an equal probability. In addition, it is assumed that the dissociation occurs much faster than the molecular rotation (axial recoil approximation), so that H^+ is ejected at spherical angles (θ_m^0, ϕ_m^0)=(54.7°, 45°) along the C-H axis in molecular frame. Furthermore, we consider that the ionization yield is proportional to the time-integration of the ionization rate, which is justified by the fact that the ionization probability is sufficiently small (< 0.1) under the present experimental conditions. The

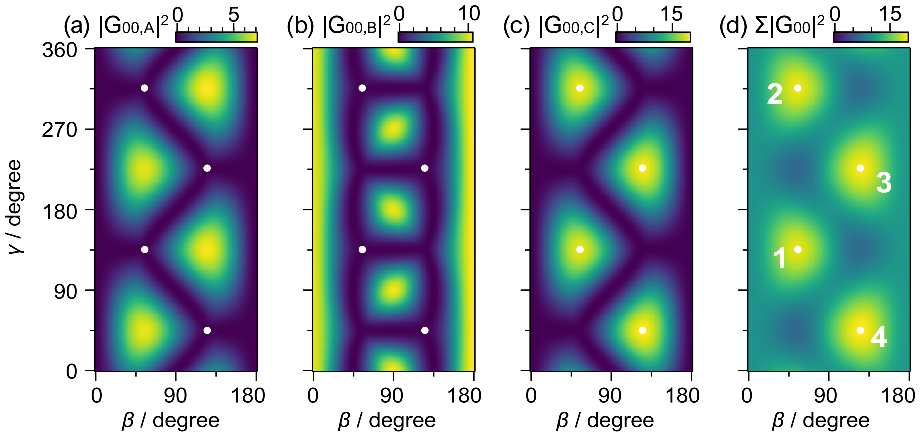

FIG. 9. Structure factors of eigenorbitals, (a) $|G_{00,\mathrm{A}}(\beta,\gamma)|^2$, (b) $|G_{00,\mathrm{B}}(\beta,\gamma)|^2$, (c) $|G_{00,\mathrm{C}}(\beta,\gamma)|^2$ and (d) the sum, $\Sigma|G_{00}(\beta,\gamma)|^2 = |G_{00,\mathrm{A}}(\beta,\gamma)|^2 + |G_{00,\mathrm{B}}(\beta,\gamma)|^2 + |G_{00,\mathrm{C}}(\beta,\gamma)|^2$ for HOMO. The dots represent the Euler angles (β, γ) at which one of the C-H axes points to the Z direction. The numbers 1-4 are the label for H atoms in the molecular frame (see Fig. 6). Note the difference in the scaling of the color bars in (a)-(d).

fragment angular distribution $P(\theta_s,\phi_s)$ in the spherical angles (θ_s,ϕ_s) is then expressed as [25],

$$P(\theta_s,\phi_s) = P(\theta_s) = \frac{1}{\sqrt{4\pi}}\sum_k c_k P_k(\cos\theta_s), \tag{13}$$

where

$$c_k = \frac{1}{\sqrt{2k+1}}\sum_q a^k_{0q} Y^*_{kq}(\theta^0_m,\phi^0_m), \tag{14}$$

$$a^k_{q'q} = (2k+1)\int P_{\mathrm{mol}}(\alpha,\beta,\gamma) D^k_{q'q}(\alpha,\beta,\gamma)\mathrm{d}\Omega, \tag{15}$$

$$P_{\mathrm{mol}}(\alpha,\beta,\gamma) = \frac{1}{8\pi^2}\int_{-\infty}^{+\infty}\Gamma(\beta,\gamma,F(t))\mathrm{d}t. \tag{16}$$

Here $P_{\mathrm{mol}}(\alpha,\beta,\gamma)$ is the angular distribution of the molecular frame (see Fig.6) and the $P_k(\cos\theta_s)$, $Y^*_{kq}(\theta^0_m,\phi^0_m)$ and $D^k_{q'q}(\alpha,\beta,\gamma)$ are the Legendre polynomial, spherical harmonics, and rotation matrix, respectively. In Eq.(15), $\int \mathrm{d}\Omega$ denotes the integration over all Euler angles, i.e., $\int \mathrm{d}\Omega = \int_0^{2\pi}\mathrm{d}\alpha\int_0^{2\pi}\mathrm{d}\gamma\int_0^{\pi}\mathrm{d}\beta\sin\beta$. The factor $1/(8\pi^2)$ in Eq.(16) is a normalization factor.

The calculated H^+ fragment angular distributions are shown in Fig.10 for relative phases ϕ = 0, π/2, and π of the ω-2ω pulse ($I_{\omega+2\omega}$ = 1.4 × 10^{14} W/cm^2 and $I_{2\omega}$ /I_ω = 0.14). The angular distribution calculated with ϕ = 0 for ϕ_{A} (Fig. 10 (a)) has a peak around θ_s = 180°. For ϕ_{C}, the distribution peaks at 0° (Fig. 10 (c)), while ϕ_{B} shows a nearly symmetric distribution (Fig. 10 (b)).

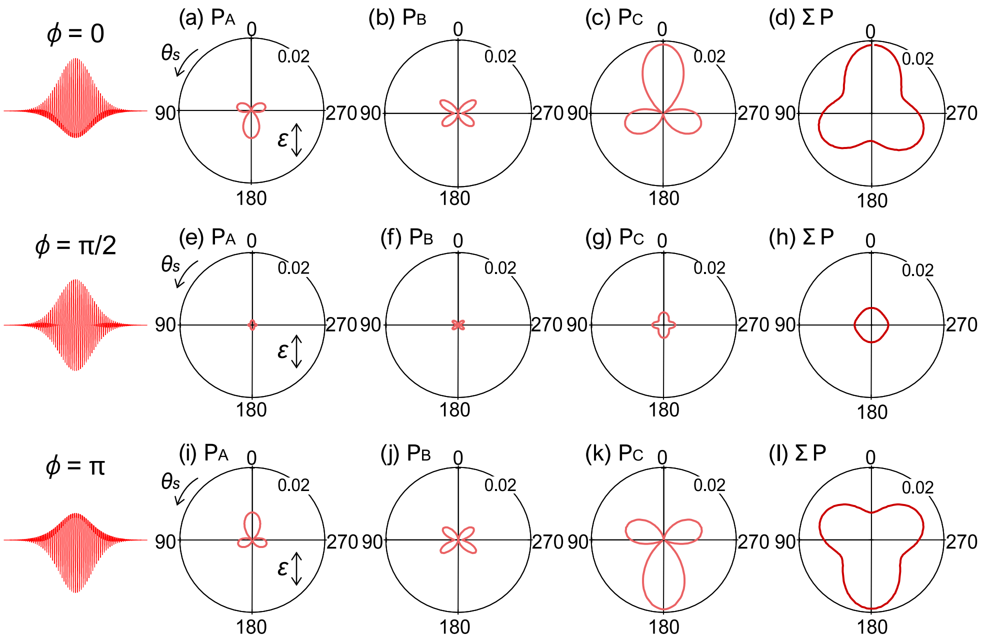

FIG. 10. Angular distributions of H^+ fragment $P_A(\theta_s)$, $P_B(\theta_s)$, and $P_C(\theta_s)$ calculated for the eigenorbitals, ϕ_A, ϕ_B, and ϕ_C for HOMO, respectively and the sum $\sum_i P_i(\theta_s) (i = A, B, C)$ in the ω-2ω laser field with the relative phase $\phi = 0$ (top row (a)-(d)), $\phi = \pi/2$ (middle row (e)-(h)), and $\phi = \pi$ (bottom row (i)-(l)).

The angular distributions for ϕ_A, ϕ_B and ϕ_C at $\phi = \pi$ (Fig. 10 (i)-(k)) form mirror images of those at $\phi = 0$. The distributions at $\phi = \pi/2$ is symmetric with respect to the laser propagation axis (θ_s = 90°, 270°) reflecting the symmetric amplitude of the laser electric field at this phase. Since the maximum amplitude of the ω-2ω laser pulse takes the smallest value at $\phi = \pi / 2$, the tunneling ionization (or the fragmentation) yield at $\phi = \pi / 2$ is smaller than those at $\phi = 0$ and π.

The total angular fragment distributions of the H^+ fragment are obtained as shown in Fig.10 (d), (h) and (l), where the three eigenorbitals are assumed equally populated. As shown in the figure, the overall features are dominated by the contributions from the eigenorbital C. The obtained results show that the H^+ fragment ion preferentially appears on the larger amplitude side of the ω-2ω laser fields [Fig.10 (d) and (l)], which is consistent with the experimental results presented in the previous section.

C. Asymmetry parameter

For a more quantitative comparison, the yields of the H (or H^+) fragment in a finite acceptance angle θ_0 around 0° and 180° are calculated as,

$$Y_+^{\theta_0}(\phi) = 2\pi \int_0^{\theta_0} P(\theta_s)\sin\theta_s \mathrm{d}\theta_s, \tag{17}$$

$$Y_-^{\theta_0}(\phi) = 2\pi \int_{\pi-\theta_0}^{\pi} P(\theta_s)\sin\theta_s \mathrm{d}\theta_s. \tag{18}$$

The asymmetry parameters defined by $A(\phi) = (Y_+(\phi) - Y_-(\phi))/(Y_+(\phi) + Y_-(\phi))$ are calculated using Eqs.(17) and (18), where $\theta_0 = 45°$ to compare with the experimental results.

The calculated asymmetry parameter for the H^+ fragment is shown in Fig.5 (b) exhibiting a clear dependence on the relative phase ϕ between the ω and 2ω laser fields. The asymmetry parameter is positive at $\phi = 0$, showing that the H^+ fragment prefers ejection to the larger amplitude side of the laser fields. The phase dependence and the amplitude of the calculated asymmetry parameter is in good agreement to the experimental result for the H^+, showing that orientation-selective tunneling ionization governs the asymmetric fragmentation of CH_4, $CH_4 \rightarrow CH_4^+ + e^-$ $\rightarrow H^+ + CH_3 + e^-$ in the ω-2ω laser fields, i.e., pathway (ii) in Eq.(4) .

V. COULOMB EXPLOSION

In this section, we discuss the Coulomb explosion pathways (I) and (II) of Eqs.(5) and (6).

A. $H^+ + CH_3^+$ pathway

The coincidence momentum image of the Coulomb explosion pathway (I) averaged over the two-color phase is shown in Fig.11 (a). The coincidence image clearly shows the feature at $|\mathbf{p}| \sim 25$ a.u. The angular distribution of H^+ with respect to the laser polarization direction is plotted in Fig.11(c), which shows an anisotropic component with $\langle\cos^2\theta\rangle = 0.82$ built on an isotropic background, which forms a ring-like feature in the momentum image. The isotropic component is attributed to the slow dissociation from the metastable state in CH_4^{2+}. The distribution of KER obtained from the momentum of the two fragment ions, $E_{\mathrm{KER}} = |\mathbf{p}_{\mathrm{H}^+}|^2/(2m_{\mathrm{H}}) + |\mathbf{p}_{\mathrm{CH}_3^+}|^2/(2m_{\mathrm{CH}_3})$ is plotted in Fig.12 (a), where $\mathbf{p}_{\mathrm{CH}_3^+}$ is the momentum of the counterpart ion, CH_3^+. The KER spectrum shows a peak at $E_{\mathrm{KER}} = 5.0$ eV with additional components at ~ 4 eV and ~ 6 eV forming tails on lower and higher energy sides.

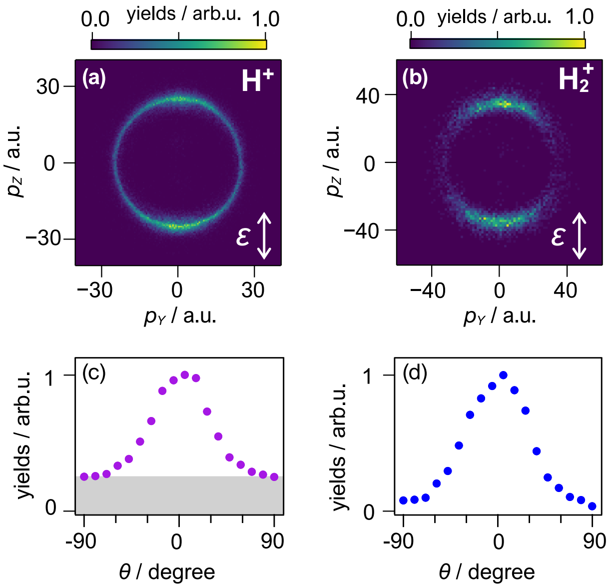

FIG. 11. Phase-averaged coincidence momentum image ($|p_X| \leq 3$ a.u.) of (a) H^+ fragment ions from $CH_4^{2+} \rightarrow H^+ + CH_3^+$ and (b) H_2^+ fragment ions from $CH_4^{2+} \rightarrow {H_2}^+ + CH_2^+$, respectively. The arrow represents the direction of the laser polarization. Angular distribution of (c) H^+ ($3 \leq E_{\mathrm{KER}} \leq 8$ eV) and (d) H_2^+ ($3 \leq E_{\mathrm{KER}} \leq 10$ eV) where the angle θ is measured with respect to the laser polarization direction. The gray area corresponds to an isotropic component.

The electronic states of CH_4^{2+} formed after removal of two-electrons from the $1t_2$ HOMO are $^3T_1$, ^1E, $^1T_2$ and $^1A_1$ in the increasing order of energy in the T_d symmetry (see Fig.3). Coulomb explosion from these dicationic states was studied previously by EUV [35, 36] and soft-X ray [33, 37] single-photon ionization as well as by electron [38, 57, 58] and ion [43, 59–61] impact ionization. The Auger electron-ion coincidence spectroscopy [37] showed that the Coulomb explosion $CH_4^{2+} \rightarrow H^+ + CH_3^+$ primarily occurs from the ^1E state of CH_4^{2+} populated by the Auger decay of C 1s core hole state. In the KER spectrum, a strong peak was observed at $E_{\mathrm{KER}} = 6$ eV with an additional component on the higher energy side forming a long tail extending up to $\sim$10 eV [33].

Based on quantum chemical calculations [33], the main peak component at 6 eV was attributed to dissociation in the ^1E state of CH_4^{2+}, which proceeds via a potential barrier in the C_{3v} geometry to the CH_3^+ product in the ^1E excited state. On the other hand, the higher energy component is assigned to dissociation from the same ^1E state dissociating to CH_3^+ in the $^1A_1$ ground state, via conical intersections to the CH_4^{2+} $^1A_1$ state [33]. The theoretical potential curves also imply that the dissociation from the higher-lying electronic state $^1T_2$ in the $(1t_2)^{-2}$ configuration can also contribute to this high energy component. This is supported by the Auger electron-ion coincidence spectroscopy [37], where a larger kinetic energy of the CH_3^+ fragment is observed for higher-lying electronic states in the $(1t_2)^{-2}$ configuration of CH_4^{2+}. The difference in the dissociation pathways appears in the recoil-frame photoelectron angular distributions (RFPAD) [33]. In particular, the RFPAD obtained with the peak KER component implies a severe breakdown of the axial-recoil approximation, which is attributed to the distortion of the molecular structure or the long dissociation lifetime of CH_4^{2+} along this pathway.

The photoion-photoion coincidence study of CH_3^+ and H^+ at $h\nu$ = 38.5 eV [36] reported additional component at a lower energy $E_{\mathrm{KER}} = 5.3\pm1.1$ eV than that of the peak component discussed above (6 eV). This was assigned to the Coulomb explosion from the lowest state in the $(1t_2)^{-2}$ configuration, $^3\mathrm{T}_1$ of CH_4^{2+} [36]. The low energy component was also observed in electron [38] and ion [60, 61] impact dissociation of methane around $E_{\mathrm{KER}} = 4.6$ eV, while the origin is yet to be understood [61].

These three components are observed in the present KER spectrum in Fig.12(a), but at slightly lower energies. For example, the main peak appears at 5.0 eV instead of 6 eV by the C 1*s* Auger decay [33]. The energy shift can be explained by the structural relaxation in CH_4^+ [62] prior to the ionization to the doubly charged states. If the reduction of the energy is sufficient to form CH_4^{2+} near the potential barrier energy along the dissociation coordinate, the dissociation lifetime would become long enough to explain the isotropic distribution observed in Figs.11(a) and (c). Indeed the metastable decay from CH_4^{2+} to H^+ and CH_3^+ has been observed in a previous study [59], where the lifetime is estimated longer than 3 μs. The formation of the long-lived highly charged parent ion is also confirmed by the time-of-flight spectrum observed in the present study (not shown), where a peak corresponding to CH_4^{2+} appears at 2.3 μs. Coulomb explosion from metastable parent ions in intense laser fields has been reported for other molecules, such as benzene [63].

Figure 12(c) presents the KER-resolved asymmetry parameter $A(\phi, E_{\mathrm{KER}})$, showing that the amplitude and the phase of the asymmetry parameter vary with the kinetic energy release E_{KER}. The asymmetry parameter exhibits clear ϕ dependences in the lower ($E_{\mathrm{KER}} \leq 4.4$ eV) and the higher ($6 \leq E_{\mathrm{KER}} \leq 8$ eV) kinetic energy regions, with a phase shift of $\sim \pi$. On the other hand, only a small phase dependence ($A_0 \leq 0.03$) is observed around the peak of the KER spectrum.

Figures 12(b) show the asymmetry parameters $A(\phi)$ integrated over the KER regions of E_{KER}

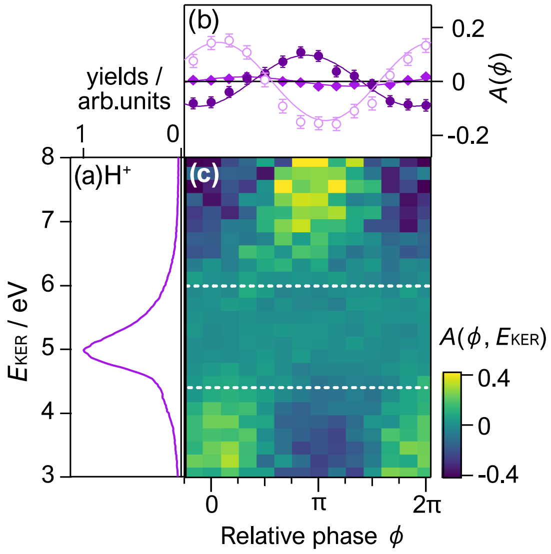

FIG. 12. (a) Total kinetic energy release E_{KER} spectra of $\mathrm{CH}_4^{2+} \to \mathrm{H}^+ + \mathrm{CH}_3^+$. (b) Phase dependence of the asymmetry parameter, $A(\phi)$ in Eq.(7), of H^+ ions for the kinetic energy ranges, $3 \le E_{\mathrm{KER}} \le 4.4$ eV (open circles), $4.4 \le E_{\mathrm{KER}} \le 6$ eV (filled diamonds), and $6 \le E_{\mathrm{KER}} \le 8$ eV (filled circles). Solid lines are numerical fits by a cosine function. (c) Two-dimensional plot of the asymmetry parameter, $A(\phi, E_{\mathrm{KER}})$ in Eq.(8), of H^+ ion.

= 3-4.4 eV, 4.4-6 eV, and 6-8 eV. The least-squares fitting analysis with $A(\phi) = A_0 \cos(\phi - \phi_0)$ shows $A_0 = 0.02(1)$, $\phi_0 = 0.3(1)\,\pi$ for the KER region of 4.4-6 eV. The small asymmetry parameter in this KER peak region can be attributed to the molecular rotation prior to the predissociation and the distortion of the molecular structure, which were discussed previously to account for the breakdown of the axial recoil approximation [33]. For the low KER region (3-4.4 eV), on the other hand, the fragment ejection shows a clear phase dependence with an asymmetry amplitude of A_0 = 0.14 (1). The phase $\phi_0 = 0.1(1)\pi$ shows that the H^+ ion is preferentially emitted to the larger amplitude side of the ω-2ω laser electric fields, while the counterpart ion, CH_3^+, is ejected in the opposite direction. The obtained phase dependence is similar to that observed for the dissociative ionization pathway (ii), showing that the orientation-selective tunneling ionization from the $1t_2$ HOMO and the further ionization to CH_4^{2+} by the electron rescattering ionization is responsible for the directional ejection for the low energy component of the pathway (I).

The asymmetry parameter for the high KER component (6-8 eV) also shows a clear phase dependence, with an amplitude of A_0 = 0.09 (1). The determined phase ϕ_0 = 0.9 (1) π, however, indicates that the H^+ ion is preferentially ejected towards the smaller electric field side of the laser fields, in the opposite direction to the low KER region. This implies that additional mechanisms other than the orientation-selective tunneling ionization from the $1t_2$ HOMO dominates the Coulomb explosion process in this high energy region. The observed phase dependence could be attributed to the contributions from tunneling ionization from $2a_1$ HOMO-1, which may have different orientation dependence from HOMO. In fact, the electronic states in the $(2a_1)^{-1}(1t_2)^{-1}$ configuration, located higher than the $(1t_2)^{-2}$ states, which can be populated by the tunneling ionization from HOMO-1 and the electron rescattering, can dissociate to CH_3^++H^+ with a small branching ratio (< 3%) [37]. Alternatively, the phase shift could be explained by the post-ionization dynamics in CH_4^{2+}, for example, in the $^1T_2$ states of the $(1t_2)^{-2}$ configuration. A possible scenario will be discussed in the next subsection.

B. H_2^+ + CH_2^+ pathway

Figure 11 (b) displays the momentum distribution of H_2^+, recorded in coincidence with CH_2^+ produced in pathway (II), $CH_4^{2+} \rightarrow H_2^+ + CH_2^+$. The momentum image exhibits a distribution peaked along the laser polarization direction. The angular distribution is shown in Fig.11(d). The fragment anisotropy $\langle \cos^2\theta \rangle$ is 0.75 for this pathway. The KER is given as $E_{\mathrm{KER}} = |\mathbf{p}_{H_2^+}|^2/(2m_{H_2}) + |\mathbf{p}_{CH_2^+}|^2/(2m_{CH_2})$, where $\mathbf{p}_{H_2^+}$ and $\mathbf{p}_{CH_2^+}$ are the momenta of H_2^+ and CH_2^+, respectively.

The two-body Coulomb explosion to CH_2^+ + H_2^+ was discussed by photoionization [36, 37], electron [38, 57, 58] and ion [43, 60] impact studies on methane. The KER spectrum in Fig.13(a) shows a broad distribution peaked at 5.2 eV, which is in good agreement with that observed in the previous study [60]. The Auger-electron-photoion coincidence spectroscopy [37] provided a secure assignment that the fragmentation proceeds from the $^1T_2$ state of CH_4^{2+} in the $(1t_2)^{-2}$ configuration, which was confirmed later by the electron impact study [38]. A recent pump-probe study [62] using a pair of intense laser pulses (800 nm, 3×10^{14} W/cm^2) has shown that Coulomb explosion from CH_4^{2+} to H_2^+ + CH_2^+ is enhanced at a later time (~20 fs) after the onset of the H^+ + CH_3^+ fragmentation. The delay was attributed to the dynamics in CH_4^+ populated by the pump laser pulse, where geometrical deformation occurs to the C_{2v} structure by the symmetry-breaking Jahn-Teller effects. The molecular dynamics simulation revealed that the H-H bond distance becomes small by the deformation, to enhance the formation of H_2^+ upon ionization by the probe pulse.

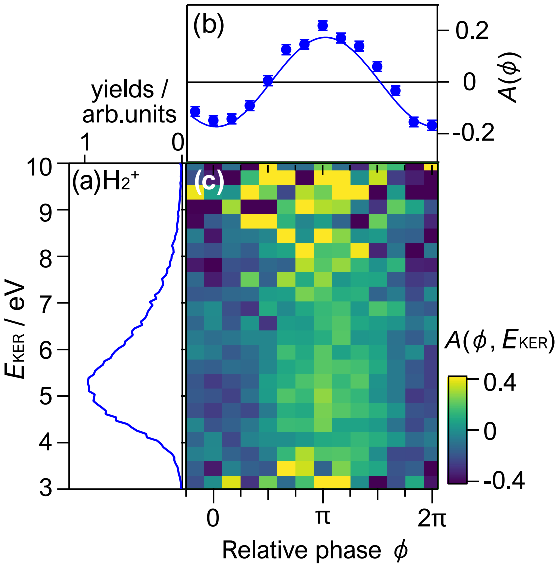

FIG. 13. (a) Total kinetic energy release E_{KER} spectra of $CH_4^{2+} \rightarrow H_2{}^+ + CH_2^+$. (b) Phase dependence of the asymmetry parameter, $A(\phi)$ in Eq.(7), of H_2^+ ions. Solid line is the result of the least-squares fitting to the cosine function in Eq.(9). (c) Two-dimensional plot of the asymmetry parameter, $A(\phi, E_{\mathrm{KER}})$ in Eq.(8), of H_2^+ ion.

This understanding of the process implies that the Coulomb explosion to the H_2^+ + CH_2^+ pathway proceeds in a similar manner. Namely, tunneling ionization from the $1t_2$ HOMO occurs first to CH_4^+, which is later ionized within the same pulse to the doubly charged $^1T_2$ state in the $(1t_2)^{-2}$ configuration to dissociate to H_2^+ + CH_2^+. Since the first ionization step favors one of the C-H bonds placed along the laser polarization direction, the H_2^+ product ejected through the Jahn-Teller distortion is expected to appear with a broader angle distribution compared with the H^+ product. This is consistent with the observed angular distribution of H_2^+, having a smaller anisotropy with $\langle \cos^2\theta \rangle = 0.75$ than $\langle \cos^2\theta \rangle = 0.82$ for the anisotropic component of pathway (I).

The asymmetry parameter for this pathway in Fig.13(b) exhibits a clear oscillation as a function of the relative phase ϕ, with $A_0 = 0.17(1)$ and $\phi_0 = 1.0(1)\ \pi$ in Eq.(9), with no significant dependence on E_{KER} as shown in Fig.13 (c). The obtained results show that the H_2^+ ions are preferentially emitted to the direction of the smaller amplitude side of the electric fields, and that the H_2^+ ejection process associated with the breaking of two C-H bonds and the bonding of two H atoms can be manipulated by the ω-2ω laser fields.

It is worth noting that the phase dependence of the asymmetry parameter $A(\phi)$ shows a large phase shift of $\sim \pi$ with respect to that expected for the tunneling ionization from the $1t_2$ HOMO (see Fig.5). In addition, the observed asymmetry amplitude $A_0 = 0.17$ is larger than that predicted by the orientation selective tunneling. These findings suggest that other processes are involved in the Coulomb explosion dynamics, which play a decisive role in determining the phase dependence. One possible mechanism is the post ionization interaction with the ω-2ω laser fields [64] leading to phase-dependent fragmentation as discussed in previous studies on CO_2^{2+} [20, 21]. In that case, the directional ejection of O^+ was identified by coincidence ion momentum imaging with CO^+ produced from CO_2 in ω-2ω intense laser fields. Since CO_2 is a symmetric molecule, the directional ejection associated with preferential breaking of one of the equivalent C-O bonds is attributed to the deformation of the potential energy surface of CO_2^{2+} in the intense laser fields [20, 21]. Indeed the phase dependence of the asymmetric bond breaking is consistent with theoretical predictions based on time-dependent adiabatic approach [65]. A similar scenario may hold for CH_4^{2+}, for example, in a molecular orientation with the C_{2v} axis placed along the laser polarization direction. It is worth noting that the higher KER component of the pathway (I) (6-8 eV) has almost the same phase dependence as pathway (II). This may indicate that these two pathways, assigned to proceed from the same electronic states $^1T_2$ share the same mechanism for the directional ejection of fragment ions from CH_4^{2+}.

VI. SUMMARY

In this study, the ω-2ω reaction control has been applied to a tetrahedral molecule CH_4. Asymmetric fragment ejections are observed in a dissociative ionization pathway ($CH_4 \rightarrow H^+ + CH_3 + e^-$) and Coulomb explosion pathways ($CH_4 \rightarrow H^+ + CH_3^+ + 2e^-$, $CH_4 \rightarrow {H_2}^+ + CH_2^+ + 2e^-$), which show clear dependences on the relative phase between the two-color fields. To understand the asymmetric fragment ejection, the tunneling ionization rates for the triply degenerated $1t_2$ HOMO were calculated by using WFAT. The fragment angular distributions and the asymmetry parameters are simulated using the WFAT tunneling rates, which showed a good agreement with the experimental results of the dissociative ionization and low energy component of the Coulomb explosion pathway to $H^+ + CH_3^+$, showing that the orientation-dependent tunneling ionization is responsible for the observed asymmetry of the fragmentation. On the other hand, the higher KER component of the H^+ Coulomb explosion pathway as well as the Coulomb explosion pathway to ${H_2}^+ + CH_2^+$, showed a clear phase shift from that expected from the orientation-dependent tunneling ionization. As a possible mechanism responsible for the phase shift, the potential deformation of the $^1T_2$ state of CH_4^{2+} is suggested. The present study demonstrated the feasibility of applying strong-field coherent control to directional fragment ejection of a symmetric polyatomic molecule with T_d symmetry. In a broader perspective, our work shows that the ω-2ω fields can provide deeper insights into the complex responses of molecules in intense laser fields through the relative phase dependences.

ACKNOWLEDGMENTS

This work was financially supported by JSPS KAKENHI Grant Numbers, JP22H00313, JP21K18929, JP19H00887, JP16H04029, MEXT Quantum Leap Flagship Program (MEXT Q-LEAP) Grant Number JPMXS0118068681 and JST SPRING Grant Number JPMJSP2125. H. H. thanks the “Interdisciplinary Frontier Next-Generation Researcher Program of the Tokai Higher Education and Research System”. O. I. T. was supported by the Ministry of Science and Higher Education of the Russian Federation (No. FSMG-2021-0005).

---

[1] A. Assion, T. Baumert, M. Bergt, T. Brixner, B. Kiefer, V. Seyfried, M. Strehle and G. Gerber, *Science*, 1998, **282**, 919–922.

[2] R. J. Levis, G. M. Menkir and H. Rabitz, *Science*, 2001, **292**, 709–713.

[3] T. Brixner and G. Gerber, *ChemPhysChem*, 2003, **4**, 418–438.

[4] E. Wells, K. J. Betsch, C. W. S. Conover, M. J. DeWitt, D. Pinkham and R. R. Jones, *Phys. Rev. A*, 2005, **72**, 063406.

[5] H. Yazawa, T. Tanabe, T. Okamoto, M. Yamanaka, F. Kannari, R. Itakura and K. Yamanouchi, *Journal of Chemical Physics*, 2006, **124**, 204314.

[6] M. Kotur, T. Weinacht, B. J. Pearson and S. Matsika, *J. Chem. Phys.*, 2009, **130**, 134311.

[7] T. Townsend, C. J. Schwartz, B. Jochim, K. R. P, T. Severt, N. Iwamoto, J. L. Napierala, P. Feizollah, S. N. Tegegn, A. Solomon, S. Zhao, K. D. Carnes, I. Ben-Itzhak and E. Wells, *Frontiers in Physics*, 2021, **9**, 691727.

[8] T. Rathje, N. G. Johnson, M. Möller, F. Süßmann, D. Adolph, M. Kübel, R. Kienberger, M. F. Kling, G. G. Paulus and A. M. Sayler, *J. Phys. B: At. Mol. Opt. Phys.*, 2012, **45**, 074003.

[9] M. F. Kling, P. von den Hoff, I. Znakovskaya and R. de Vivie-Riedle, *Phys. Chem. Chem. Phys.*, 2013, **15**, 9448–9467.

[10] M. Kremer, B. Fischer, B. Feuerstein, V. L. B. de Jesus, V. Sharma, C. Hofrichter, A. Rudenko, U. Thumm, C. D. Schröter, R. Moshammer and J. Ullrich, *Phys. Rev. Lett.*, 2009, **103**, 213003.

[11] H. Xu, T.-Y. Xu, F. He, D. Kielpinski, R. T. Sang and I. V. Litvinyuk, *Phys. Rev. A*, 2014, **89**, 041403.

[12] I. Znakovskaya, P. von den Hoff, G. Marcus, S. Zherebtsov, B. Bergues, X. Gu, Y. Deng, M. J. J. Vrakking, R. Kienberger, F. Krausz, R. de Vivie-Riedle and M. F. Kling, *Phys. Rev. Lett.*, 2012, **108**, 063002.

[13] M. F. Kling, C. Siedschlag, A. J. Verhoef, J. I. Khan, M. Schultze, T. Uphues, Y. Ni, M. Uiberacker, M. Drescher, F. Krausz and M. J. J. Vrakking, *Science*, 2006, **312**, 246–248.

[14] P. von den Hoff, I. Znakovskaya, M. Kling and R. de Vivie-Riedle, *Chem. Phys.*, 2009, **366**, 139–147.

[15] M. Kübel, C. Burger, R. Siemering, N. G. Kling, B. Bergues, A. S. Alnaser, I. Ben-Itzhak, R. Moshammer, R. de Vivie-Riedle and M. F. Kling, *Mol. Phys.*, 2017, **115**, 1835–1845.

[16] B. Sheehy, B. Walker and L. F. DiMauro, *Phys Rev Lett*, 1995, **74**, 4799–4802.

[17] H. Ohmura, T. Nakanaga and M. Tachiya, *Phys. Rev. Lett.*, 2004, **92**, 113002.

[18] D. Ray, F. He, S. De, W. Cao, H. Mashiko, P. Ranitovic, K. P. Singh, I. Znakovskaya, U. Thumm, G. G. Paulus, M. F. Kling, I. V. Litvinyuk and C. L. Cocke, *Phys. Rev. Lett.*, 2009, **103**, 223201.

[19] V. Wanie, H. Ibrahim, S. Beaulieu, N. Thiré, B. E. Schmidt, Y. Deng, A. S. Alnaser, I. V. Litvinyuk, X.-M. Tong and F. Légaré, *J. Phys. B: At. Mol. Opt. Phys.*, 2015, **49**, 025601.

[20] T. Endo, H. Fujise, A. Matsuda, M. Fushitani, H. Kono and A. Hishikawa, *J. Electron Spectroc. Relat. Phenom.*, 2016, **207**, 50–54.

[21] T. Endo, H. Fujise, Y. Kawachi, A. Ishihara, A. Matsuda, M. Fushitani, H. Kono and A. Hishikawa, *Phys. Chem. Chem. Phys.*, 2017, **19**, 3550–3556.

[22] Q. Song, X. Gong, Q. Ji, K. Lin, H. Pan, J. Ding, H. Zeng and J. Wu, *J. Phys. B: At. Mol. Opt. Phys.*, 2015, **48**, 094007.

[23] E. Kechaoglou, S. Kaziannis and C. Kosmidis, *Phys. Chem. Chem. Phys.*, 2019, **21**, 11259–11265.

[24] E. Kechaoglou, K. Ferentinou, S. Kaziannis and C. Kosmidis, *J. Chem. Phys.*, 2021, **154**, 244306.

[25] H. Hasegawa, T. Walmsley, A. Matsuda, T. Morishita, L. B. Madsen, F. Jensen, O. I. Tolstikhin and A. Hishikawa, *Front. Chem.*, 2022, **10**, 857863.

[26] H. Fujise, M. Uemura, H. Hasegawa, D. Ikeya, A. Matsuda, T. Morishita, L. B. Madsen, F. Jensen, O. I. Tolstikhin and A. Hishikawa, *Phys. Chem. Chem. Phys.*, 2022, **24**, 8962–8969.

[27] O. I. Tolstikhin, T. Morishita and L. B. Madsen, *Phys. Rev. A*, 2011, **84**, 053423.

[28] T. Endo, A. Matsuda, M. Fushitani, T. Yasuike, O. I. Tolstikhin, T. Morishita and A. Hishikawa, *Phys. Rev. Lett.*, 2016, **116**, 163002.

[29] W. Quan, M. Yuan, S. Yu, S. Xu, Y. Chen, Y. Wang, R. Sun, Z. Xiao, C. Gong, L. Hua, X. Lai, X. Liu and J. Chen, *Opt. Exp.*, 2016, **24**, 23248.

[30] H. Li, D. Ray, S. De, I. Znakovskaya, W. Cao, G. Laurent, Z. Wang, M. F. Kling, A. T. Le and C. L. Cocke, *Phys. Rev. A*, 2011, **84**, 043429.

[31] H. Hasegawa, A. Hishikawa and K. Yamanouchi, *Chem. Phys. Lett.*, 2001, **349**, 57–63.

[32] S. Xu, X. Ma, X. Ren, A. Senftleben, T. Pflüger, A. Dorn and J. Ullrich, *Phys. Rev. A*, 2011, **83**, 052702.

[33] J. B. Williams, C. S. Trevisan, M. S. Schöffler, T. Jahnke, I. Bocharova, H. Kim, B. Ulrich, R. Wallauer, F. Sturm, T. N. Rescigno, A. Belkacem, R. Dörner, T. Weber, C. W. McCurdy and A. L. Landers, *J. Phys. B: At. Mol. Opt. Phys.*, 2012, **45**, 194003.

[34] J. Appell and C. Kubach, *Chem. Phys. Lett.*, 1971, **11**, 486–490.

[35] S. Leach, *J. Mol. Struct.*, 1987, **157**, 197–214.

[36] G. Dujardin, D. Winkoun and S. Leach, *Phys. Rev. A*, 1985, **31**, 3027–3038.

[37] E. Kukk, G. Prümper, R. Sankari, M. Hoshino, C. Makochekanwa, M. Kitajima, H. Tanaka, H. Yoshida, Y. Tamenori, E. Rachlew and K. Ueda, *J. Phys. B: At. Mol. Opt. Phys.*, 2007, **40**, 3677–3692.

[38] R. Flammini, M. Satta, E. Fainelli, G. Alberti, F. Maracci and L. Avaldi, *New J. Phys.*, 2009, **11**, 083006.

[39] J. Strohaber, F. Zhu, A. A. Kolomenskii and H. A. Schuessler, *Phys. Rev. A*, 2014, **89**, 023430.

[40] S. Wang, X. Tang, L. Gao, M. E. Elshakre and F. Kong, *J. Phys. Chem.*, 2003, **107**, 6123–6129.

[41] Z. Wu, C. Wu, Q. Liang, S. Wang, M. Liu, Y. Deng and Q. Gong, *J. Chem. Phys.*, 2007, **126**, 074311.

[42] P. Plessis, P. Marmet and R. Dutil, *J. Phys. B: At. Mol. Phys.*, 1983, **16**, 1283–1294.

[43] W. J. Griffiths, S. Svensson, A. N. d. Brito, N. Correia, M. L. Langford and F. M. Harris, *Rapid Commun. Mass Spectrom.*, 1992, **6**, 438–448.

[44] M. Sharifi, F. Kong, S. L. Chin, H. Mineo, Y. Dyakov, A. M. Mebel, S. D. Chao, M. Hayashi and S. H. Lin, *J. Phys. Chem. A*, 2007, **111**, 9405–9416.

[45] A. J. Illies, M. F. Jarrold and M. T. Bowers, *J. Am. Chem. Soc.*, 1982, **104**, 3587–3593.

[46] S. Xu, X. Ma, X. Ren, A. Senftleben, T. Pflüger, S. Yan, P. Zhang, J. Yang, J. Ullrich and A. Dorn, *J. Chem. Phys.*, 2013, **138**, 134307.

[47] R. Dixon, *Mol. Phys.*, 1971, **20**, 113–126.

[48] L. B. Madsen, O. I. Tolstikhin and T. Morishita, *Phys. Rev. A*, 2012, **85**, 053404.

[49] R. N. Zare, *Angular Momentum*, Wiley, New York, 1988.

[50] M. W. Schmidt, K. K. Baldridge, J. A. Boatz, S. T. Elbert, M. S. Gordon, J. H. Jensen, S. Koseki, N. Matsunaga, K. A. Nguyen, S. Su, T. L. Windus, M. Dupuis and J. A. Montgomery, *J. Comput. Chem.*, 1993, **14**, 1347–1363.

[51] B. M. Bode and M. S. Gordon, *J. Mol. Graph. and Model.*, 1998, **16**, 133–138.

[52] P. M. Kraus, O. I. Tolstikhin, D. Baykusheva, A. Rupenyan, J. Schneider, C. Z. Bisgaard, T. Morishita, F. Jensen, L. B. Madsen and H. J. Wörner, *Nat. Commun.*, 2015, **6**, 7039.

[53] A. I. Dnestryan and O. I. Tolstikhin, *Phys. Rev. A*, 2016, **93**, 033412.

[54] L. B. Madsen, F. Jensen, A. I. Dnestryan and O. I. Tolstikhin, *Phys. Rev. A*, 2017, **96**, 013423.

[55] A. I. Dnestryan, O. I. Tolstikhin, L. B. Madsen and F. Jensen, *J. Chem. Phys.*, 2018, **149**, 164107.

[56] F. Jensen, *J. Chem. Phys.*, 2001, **115**, 9113–9125.

[57] R. Singh, P. Bhatt, N. Yadav and R. Shanker, *Phys. Rev. A*, 2013, **87**, 062706.

[58] B. Wei, Y. Zhang, X. Wang, D. Lu, G. C. Lu, B. H. Zhang, Y. J. Tang, R. Hutton and Y. Zou, *J. Chem. Phys.*, 2014, **140**, 124303.

[59] P. G. Fournier, J. Fournier, F. Salama, P. J. Richardson and J. H. D. Eland, *J. Chem. Phys.*, 1985, **83**, 241–246.

[60] Y. Zhang, B. Wang, L. Wei, T. Jiang, W. Yu, R. Hutton, Y. Zou, L. Chen and B. Wei, *J. Chem. Phys.*, 2019, **150**, 204303.

[61] J. Rajput, D. Garg, A. Cassimi, A. Méry, X. Fléchard, J. Rangama, S. Guillous, W. Iskandar, A. N. Agnihotri, J. Matsumoto, R. Ahuja and C. P. Safvan, *J. Chem. Phys.*, 2022, **156**, 054301.

[62] M. Li, M. Zhang, O. Vendrell, Z. Guo, Q. Zhu, X. Gao, L. Cao, K. Guo, Q.-Q. Su, W. Cao, S. Luo, J. Yan, Y. Zhou, Y. Liu, Z. Li and P. Lu, *Nat. Commun.*, 2021, **12**, 4233.

[63] A. Matsuda, M. Fushitani, R. A. Thomas, V. Zhaunerchyk and A. Hishikawa, *Journal of Physical Chemistry A*, 2009, **113**, 2254–2260.

[64] T. Endo, K. M. Ziems, M. Richter, F. G. Fröbel, A. Hishikawa, S. Gräfe, F. Légaré and H. Ibrahim, *Front. Chem.*, 2022, **10**, 8597501.

[65] Y. Sato, H. Kono, S. Koseki and Y. Fujimura, *J. Am. Chem. Soc.*, 2003, **125**, 8019–8031.